Bridged Bowtie Aperture Antenna for Producing an Electromagnetic Hot Spot

Yang Chen,[†] Yuhang Chen,[†] Jiaru Chu,*[,†] and Xianfan Xu*[,‡]

[†]Department of Precision Machinery and Precision Instruments, University of Science and Technology of China, Hefei City, Anhui Province 230026, China

[‡]School of Mechanical Engineering and Birck Nanotechnology Center, Purdue University, West Lafayette, Indiana 47907, United States

S *Supporting Information*

ABSTRACT: In this work we report a new type of nanostructure, the bridged bowtie aperture (BBA) antenna, for producing a simultaneously enhanced and confined electric and magnetic near field. The optical nanocircuit theory is employed to reveal its underlying mechanism. The electric near-field distribution of the nanostructure is observed using transmission-type s-SNOM at the nanoscale, and the magnetic near-field distribution is then derived from the electric near field of a complementary BBA structure using Babinet's principle. To our knowledge, the generation of such an electromagnetic hot spot has never been experimentally demonstrated. Relative to the existing nanostructures that can produce an electromagnetic hot spot, the BBA antenna has apparent advantages, which offers a new approach for nonlinear optics, surface-enhanced spectroscopy, biosensing, and metamaterials.

KEYWORDS: *nanoantenna, surface plasmon, electromagnetic field localization, Babinet's principle, scanning near-field optical microscopy*
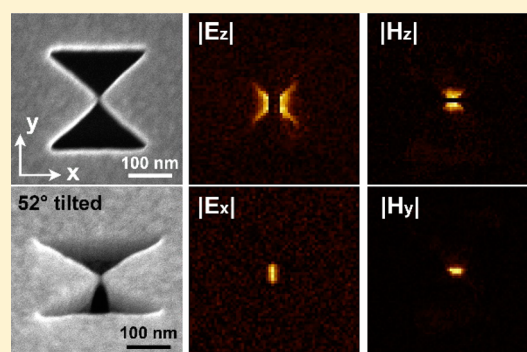
$\mathbf{P}$lasmonic antennas have attracted extensive interest for their ability to control and manipulate the optical field at the nanoscale.[1−4] Derived from the Maxwell equations, the force applied to a charge by the electric field is c/v larger than that exerted by the magnetic field, where c is the speed of light and v is the velocity of the charge. As a consequence, the response of a material to an electric field described by the electric permittivity is a factor of 10^4 stronger than that to a magnetic field described by the magnetic permeability.[5] Thus, most of the plasmonic antennas are designed to manipulate the electric component of light. Meanwhile, other types of antennas are also developed to create localized and enhanced magnetic fields, such as diabolo nanoantennas,[6] complementary bowtie apertures,[7] and plasmonic oligomers.[8]

Recently, a number of new types of plasmonic antennas are proposed to simultaneously enhance and confine electric and magnetic fields, which can greatly extend the applicability and flexibility of nanoantennas.[9−11] In nonlinear optics, an enhanced electric field is usually employed for the second-harmonic or third-harmonic generation.[12,13] Meanwhile, the local magnetic field associated with the magnetic-dipole resonance of the nanoantenna can also be utilized to generate the second-harmonic light.[14] Thus, it is possible to apply the simultaneously enhanced electric and magnetic fields to nonlinear optics. In addition, in the metamaterial research, it has been demonstrated that both the electric and magnetic

responses are important to realize specific performances, such as negative refractive index[15,16] and enhanced near-field radiative heat transfer.[17] Accordingly, the electromagnetic hot spot may find applications in metamaterials. However, no experimental results have ever been demonstrated to support the generation of such an electromagnetic hot spot mainly due to two difficulties: the fabrication of samples and the simultaneous measurement of the electric and magnetic near-field distribution at the nanoscale.

In this work, we present a novel bridged bowtie aperture (BBA) antenna for producing an electromagnetic hot spot. The optical nanocircuit theory is introduced to reveal its physical mechanism. Scattering-type scanning near-field microscopy (s-SNOM) is used to obtain the amplitude- and phase-resolved electric near-field distribution of BBA antennas with varied geometrical parameters. Then the electromagnetic complement of the BBA antenna is fabricated and scanned using s-SNOM, and the magnetic near-field distribution of the BBA antenna is obtained by applying Babinet's principle. The experimental results agree well with the simulations. It is found that this new type of nanoantenna can be a desirable nanostructure to simultaneously enhance and confine electric and magnetic
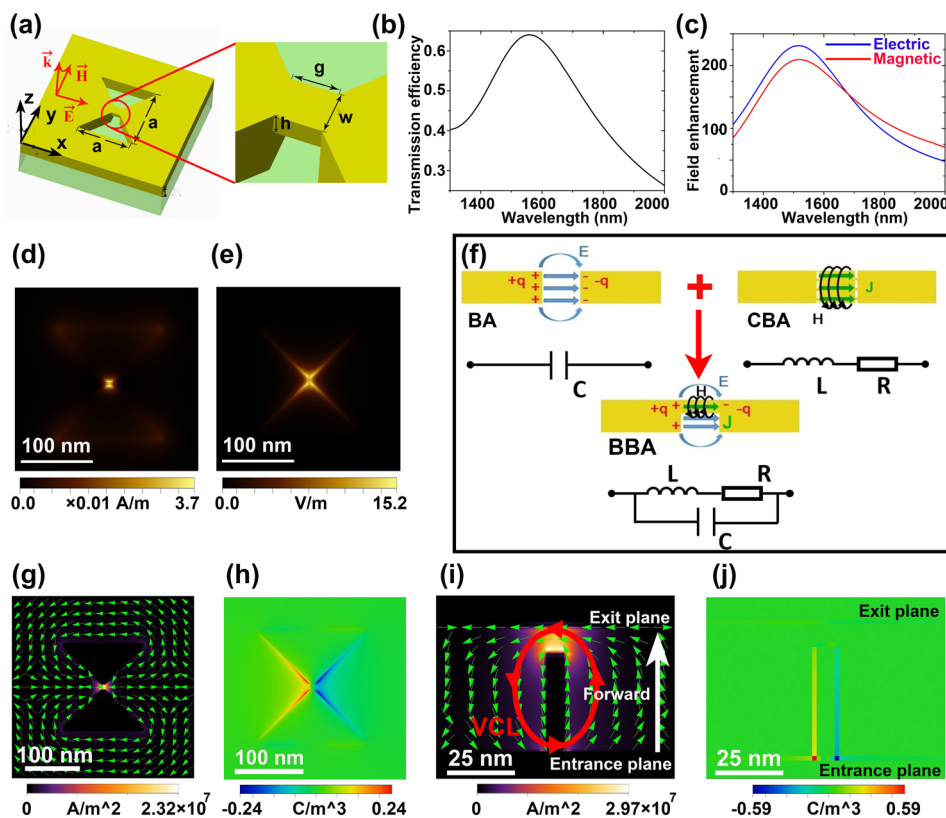
Figure 1. (a) Schematic of a bridged bowtie aperture antenna. (b) Simulated transmission spectrum of the structure. The transmission efficiency is defined as transmitted intensity integrated over the aperture area normalized by the incident intensity integrated over the same area. (c) Simulated electric and magnetic field intensity enhancement monitored 4 nm above the center of the bridge. (d, e) Magnetic and electric near-field distribution plotted at 4 nm above the exit plane at 1560 nm. (f) Theoretical description of the bowtie aperture, the complementary bowtie aperture, and the BBA antenna based on the optical nanocircuit theory. (g, i) Simulated induced current distribution at the exit plane and the $x-z$ cross section at 1560 nm. The background brightness and arrows respectively indicate the magnitude and direction of the induced current. (h, j) Simulated surface charge distribution at the exit plane and the $x-z$ cross section at 1560 nm.

fields, which promises potential applications in SERS,[18,19] nonlinear optics,[20,21] metamaterials,[22,23] and biosensing.[24,25]

■ RESULTS AND DISCUSSION

Plasmonic Interaction in the Bridged Bowtie Aperture Antenna. A typical BBA antenna shown in Figure 1a consists of a bowtie aperture (the aperture size $a = 210$ nm) connected with a metal bridge (width $w = 10$ nm, length $g = 10$ nm, thickness $h = 10$ nm) at the gap area on the exit plane. The structure is fabricated in a gold film (thickness $H = 60$ nm) on a suspended Si_3N_4 substrate using the backside milling method.[26] An excitation laser with proper polarization is incident from the lower side of the aperture, i.e., the entrance side, transmitted by the aperture, and then radiated into the upper side, i.e., the exit side. Its electric component is 1 V/m, and its magnetic component is 0.00253 A/m. Calculating its transmission spectrum using the finite difference time domain method (Lumerical FDTD Solutions), we observe a transmission resonance at 1560 nm, where the electric and magnetic fields get their maximum enhancement as shown in Figure 1b and c. The influence of the structural parameters on the transmission resonance is computed and shown in Supplementary Figure 1.

As depicted in Figure 1d and e, both the magnetic and the electric field of the BBA antenna are enhanced and confined at its central area. For the sake of simplicity and clarity, this kind of simultaneously enhanced and confined electric and magnetic near field is termed *electromagnetic hot spot* here. The

generation of the electromagnetic hot spot can be analyzed using the optical nanocircuit theory[27,28] as depicted in Figure 1f. If the metal bridge is removed, the BBA antenna is converted to a bowtie aperture,[29] where charges with opposite signs pile up at the two sides of the air gap, generating an electric hot spot, but no magnetic hot spot. Here, the gap is electrically isolated and acts as a capacitor C. Once the two sides across the gap are connected by a metal bridge, part of the accumulated charges funnel through the bridge and convert to a confined and enhanced current as shown in Figure 1g. On the basis of Ampere's law, the magnetic near field, enhanced and localized, is azimuthally polarized around the bridge as shown in Figure 1d. Meanwhile, the thickness of the bridge limits its ability to deliver all the charges through it. Thus, there are considerable charges with opposite signs remaining at aperture edges right beside the two terminals of the bridge as shown in Figure 1h, producing a confined and enhanced electric field at the center area as depicted in Figure 1e. On the xz plane, a virtual current loop (VCL) is formed in the forward direction as shown in Figure 1i, which is composed of two oppositely induced currents generated at the two sidewalls of the gap, the charge currents through the metal bridge on the exit plane, and the displacement current across the air gap.[30] The formed VCL behaves as a magnetic dipole and effectively delivers induced current from the entrance plane to the exit plane and then through the metal bridge.[31,32] Besides, considerable charges are deposited on the two sidewalls below the bridge as shown in
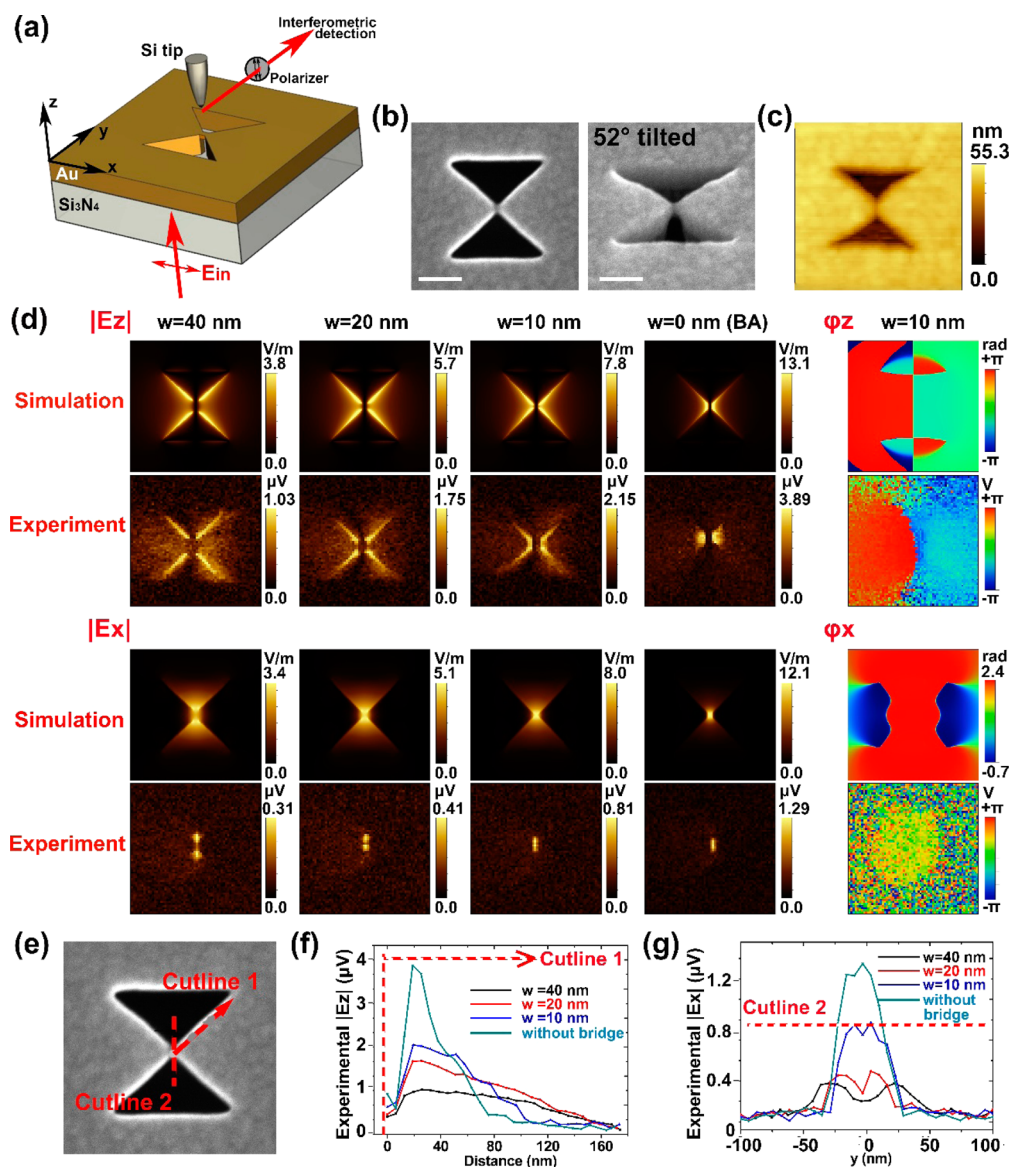
Figure 2. (a) Experimental setup for the near-field imaging in the transmission mode. (b) SEM images of a BBA antenna sample (scale bar: 100 nm). (c) Topography of the sample measured by AFM. (d) Calculated and experimental electric near-field amplitude and phase distribution of E_z and E_x for BBA antennas with different bridge width w ($a = 210$ nm, $g = h = 20$ nm). (Image size of the AFM image and electric field images: 390 nm × 390 nm.) (e) Schematic of the two cutlines. (f) $|E_z|$ distribution along the cutline 1 extracted from (d). (g) $|E_x|$ distribution along the cutline 2 extracted from (d).

Figure 1j. Thus, the gap load can be described as a parallel circuit composed of an inductive impedance L of the metal bridge and a capacitive impedance C of the dielectric material below the bridge. A resistance impedance R is in series connection with the inductor L to represent the dissipation effect of the metal bridge. If the bridge has the same thickness as the metal film, the BBA antenna transforms to a complementary bowtie aperture (CBA),[7] where all or most of the accumulated charges flow through the bridge, producing a magnetic hot spot, but no or a very weak electric hot spot. Then, the gap is electrically conductive and acts as an inductor L in series with a resistor R.

Experimental Measurements and Numerical Simulations of the Electric Near-Field Distribution. Transmission-type scattering scanning near-field optical microscopy is utilized to visualize the electric field distribution of the BBA antenna in real space as shown in Figure 2a. A plane wave at

1550 nm with proper polarization is illuminated from below the sample. Light scattered by the dielectric silicon tip scanning over the sample is collected and analyzed using higher-harmonic demodulation[33] and pseudoheterodyne interferometry.[34] SEM and AFM images of a fabricated BBA are shown in Figure 2b and c.

As shown in Figure 2d, for the BBA antenna with a wide bridge ($w = 40$ nm), most of the accumulated charges funnel through the bridge, with the remaining charges located loosely along the aperture edges. As a result, four hot bars along the edges are observed for the longitudinal components $|E_z|$, together with two hot spots on two sides of the bridge for the transverse components $|E_x|$. As the bridge becomes narrower, its ability to deliver surface current is weakened and the gap load is getting more capacitive,[27] leaving increased charges localized along the edges and squeezed toward the bridge. As a consequence, the four hot bars of $|E_z|$ are continuously
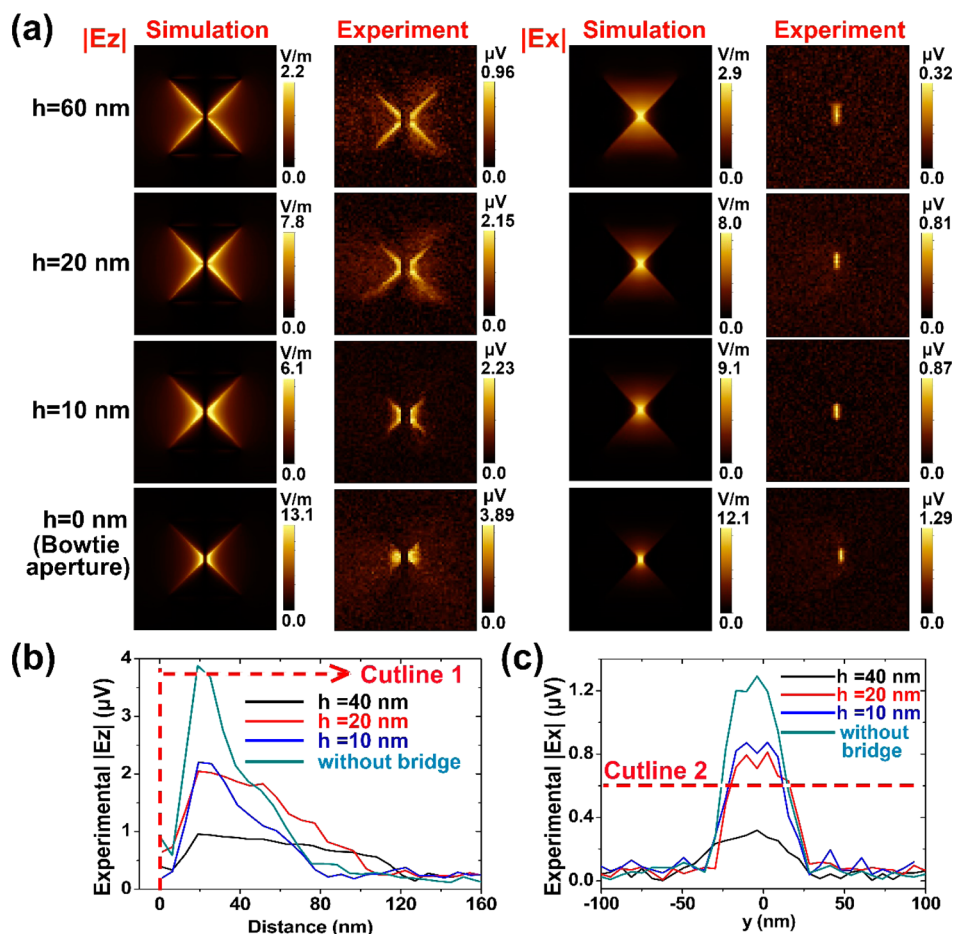
Figure 3. (a) Calculated and experimental electric near-field distribution of |E_z| and |E_x| for BBA antennas with different bridge thickness h (a = 210 nm, g = 20 nm, w = 10 nm) and the bowtie aperture. (Image size of the AFM image and electric field images: 390 nm × 390 nm.) (b) |E_z| distribution along cutline 1 extracted from (a). (c) |E_x| distribution along cutline 2 extracted from (a).

enhanced and compressed to the center of the aperture and finally combined into two hot spots (w = 10 nm) just like the bowtie aperture. As to the |E_x| component, the two hot spots fuse into one with decreasing bridge width w, and the near-field amplitude is substantially enhanced. Simulation results give an electric field intensity enhancement of 124 for w = 10 nm. To further demonstrate the impact of the bridge width w on the near-field distribution, the electric fields along two cutlines as shown in Figure 2e are analyzed. The |E_z| magnitude on cutline 1 along the aperture edge and the |E_x| magnitude on cutline 2 across the bridge are extracted from the experimental data and compared in Figure 2f,g. Field sizes of 68 and 45 nm (fwhm) are achieved respectively on cutline 1 and 2 for the bridge width of 10 nm. Apparently, a narrow metal bridge is critical to produce a highly enhanced and localized electric field for the BBA antenna. Considering the phase distribution (the rightmost column of Figure 2d), a phase jump of π is observed in the φ_z plot across the central line of the BBA antenna in simulation, because surface charges accumulating at the two sides of the bridge have opposite signs and act like an electric dipole.[26] The experimental results also show a π phase shift across the central line. As to the in-plane component φ_x, it is continuous across the bridge, as seen in both simulation and experimental results.

To further analyze the electric near-field enhancement and localization of the BBA antenna, the influence of the metal bridge thickness h is varied as shown in Figure 3a. The bridge

width w is fixed as 10 nm. With decreasing h, the ability of the metal bridge to carry surface current is weakened and the gap load becomes more capacitive. As a result, more charges are gathered at the aperture edges and compressed toward the center of the aperture, leading to a more enhanced and confined near-field distribution, which is clearly demonstrated in the cutline curves in Figure 3b,c. The definition of the cutlines is the same as that in Figure 2e. With an ultrathin bridge (h = 10 nm), field sizes of 38 and 41 nm (fwhm) are realized respectively on cutlines 1 and 2 extracted from the experimental data, which are comparable to that of 31 and 37 nm for the bowtie aperture (h = 0). The electric field intensity enhancement of 132 is achieved based on simulations. Note that the BBA antenna with a bridge thickness of 10 nm is not excited resonantly at 1550 nm, and thus the enhancement of 132 can be further increased by adjusting the excitation laser to resonance wavelength.

Experimental Measurements and Numerical Simulations of the Magnetic Near-Field Distribution. Mapping the magnetic near-field distribution at the nanoscale has long been challenging, especially for the plasmonic structures such as BBA antennas, which can produce a magnetic field with a size of less than 50 nm. Vector-resolved electric near-field measurement using s-SNOM can be used to figure out the magnetic field distribution based on Maxwell's equation,[35−37] but the process of data acquisition and data interpretation can be quite complex and difficult. Aperture-type near-field imaging
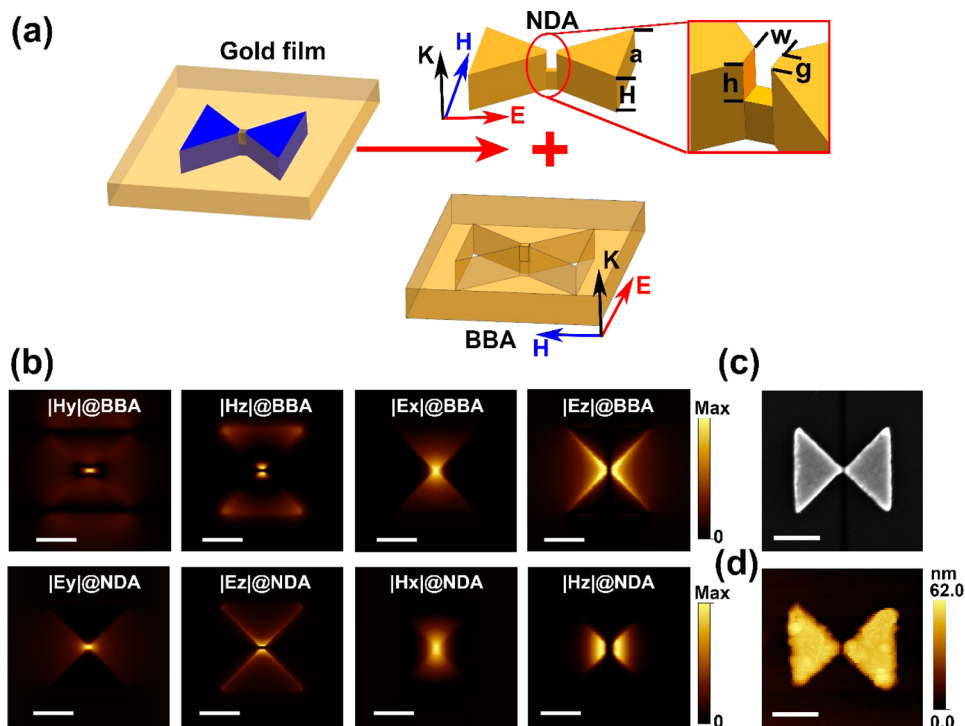
Figure 4. (a) Schematic of the electromagnetic complementary relationship between the BBA antenna and the NDA antenna based on Babinet's principle (inset: the magnified image of the notch). (b) Magnetic and electric field distribution of the BBA antenna compared with the electric and magnetic field distribution of NDA plotted at 4 nm above the antennas at 1560 nm (a = 210 nm, g = 20 nm, w = h = 10 nm). (c) SEM image of an NDA antenna. (d) AFM image of an NDA antenna. (Scale bar in c−e is 100 nm.)

can also probe the magnetic field,[38−41] but its spatial resolution cannot resolve the highly confined magnetic field generated by the BBA antenna. Moreover, specially prepared probes and numerical modeling are required for these methods. As an alternative, Babinet's principle provides a means to determine the magnetic field of an optical antenna.[42,43] Originating from the classical optics, Babinet's principle has been extended as an approximation for metamaterials with a finite thickness over a broad spectrum (from RF to IR),[44,45] providing a theoretical link between the electric (magnetic) field of an electromagnetic structure and the magnetic (electric) field of its complementary structure. Figure 4a shows the relationship between the BBA antenna and its electromagnetic complement, a notched diabolo antenna (NDA) with a notch at its center. Although the structures of the BBA and NDA do not completely fulfill the requirements of Babinet's principle due to their quasi-3D structure, the magnetic and electric field distributions of the BBA antenna are similar to the electric and magnetic field distributions of the NDA, respectively, as shown in Figure 4b. Thus, Babinet's principle can be applied as an approximation for such a quasi-3D plasmonic structure in the near-IR spectrum. Based on this, the magnetic field distribution of the BBA antenna can be derived from the electric field distribution of the NDA, which can be visualized using s-SNOM. The fabrication process of the NDA sample is described in the Methods section. The SEM image and AFM image of a NDA sample are shown in Figure 4c,d.

As discussed before, the gap load of the BBA antenna becomes more capacitive with decreasing bridge width w, and the total current funneling through the bridge is accordingly reduced. Meanwhile, the cross section of the bridge is also decreased, leading to a more confined induced current. The impact of these two factors on the magnetic field intensity is

competing, and the effect of the shrinking cross section is dominant. Thus, the BBA antenna with a narrower bridge produces a more enhanced and confined magnetic field as shown in Figure 5a. Such a localized magnetic field is azimuthally polarized around the bridge, which is clearly supported by its phase information in Figure 5a. As its electromagnetic complement, the NDA has a similar electric field distribution to the magnetic field distribution of the BBA antenna, and their dependence on the width w is identical. But for the bowtie aperture antenna with no bridge (w = 0 nm), the magnetic field is distributed in the two arms with no field localization. Corresponding to the bowtie aperture, the diabolo antenna with no notch (w = 0 nm) produces a dispersed electric field. The experimental results of the NDA using s-SNOM agree well with the simulations as shown in Figure 5a. One hot spot is observed for the E_y component, with a continuous phase signal across the notch. For the E_z component, two adjacent hot spots on each side of the notch are observed with a phase jump of about π. Besides, its electric field is more enhanced and confined with a reduced notch width w, which is apparently present in the cutline curves in Figure 5b,c. The cutline is extracted from the experimental data along the y direction across the center of the bridge. Field sizes of 15.5 and 15.1 nm are achieved respectively for the E_z and E_x component at w = 10 nm. Simulation results give a magnetic field intensity enhancement of 90 for w = 10 nm. According to Babinet's principle, the BBA antenna can produce an enhanced and confined magnetic hot spot at its central area. Note that the electric field pattern of the diabolo antenna without a notch is mainly attributed to the imperfections of the sample.

Optimization of Structural Parameters of the BBA Antenna. In order to optimize structural parameters of the BBA antenna, the magnetic near field is monitored 4 nm above
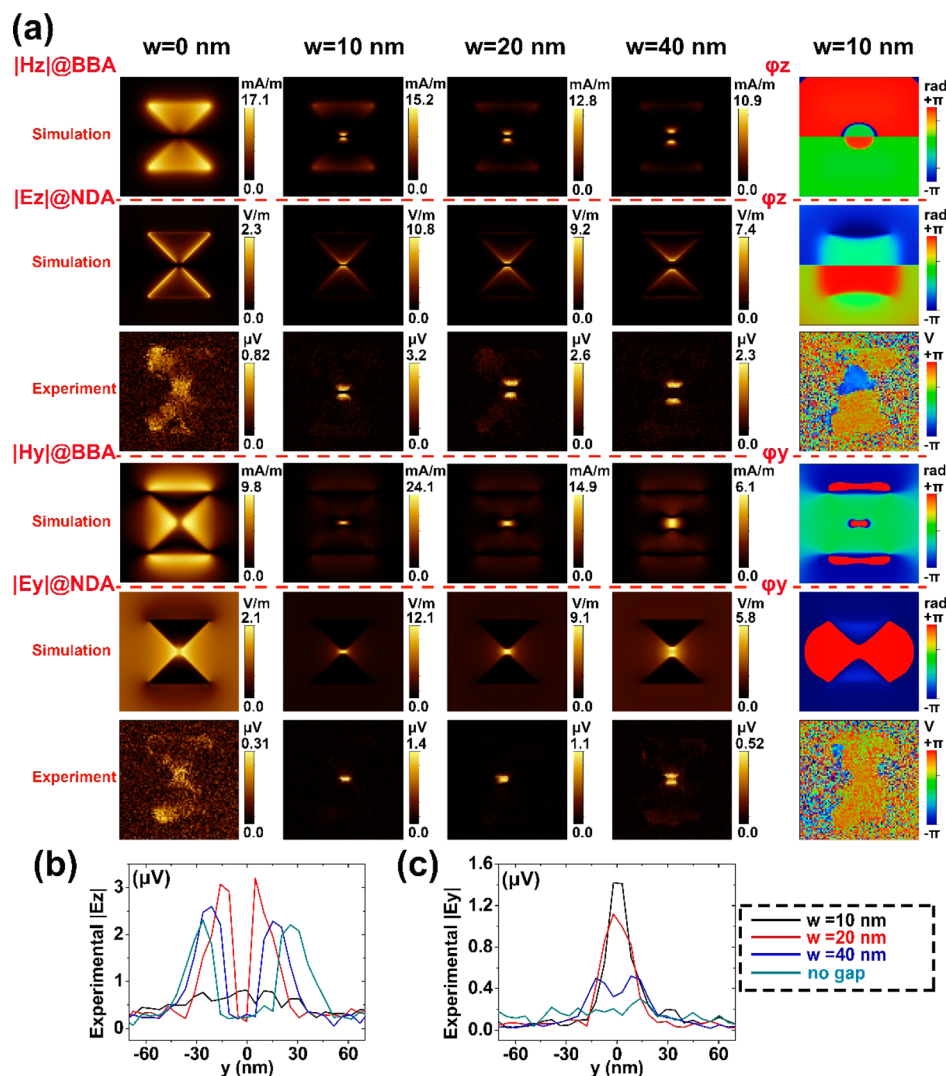
Figure 5. (a) Calculated magnetic near-field distribution of the BBA antenna together with the calculated and experimental electric near-field distribution of the corresponding NDA antenna with different width w ($a = 210$ nm, $g = 20$ nm, $h = 10$ nm). (Image size of the AFM image and the electric/magnetic field images: 390 nm × 390 nm.) (b, c) $|E_z|$ and $|E_x|$ distributions along the cutline extracted from (a).

the center of the metal bridge with different bridge length g, bridge width w, and bridge thickness h. For a bowtie aperture, more charges accumulate at the two sides of the air gap for a smaller gap size g.[46] Then if a metal bridge is established, more charges will flow through the bridge correspondingly, producing a more enhanced magnetic near field as shown in Figure 6a. As to the bridge width w and bridge thickness h, the decrease of the two parameters will intensify the magnetic field as a result of shrinking cross section, which has been discussed before. However, this kind of dependence is reversed as the two parameters decrease below 10 nm, because the electromagnetic field penetrates completely into the metal bridge and then the dissipation effect starts to take over.[47] With optimized structural parameters ($g = 5$ nm, $w = 10$ nm, $h = 10$ nm), a magnetic field enhancement of 118 is achieved together with an electric field enhancement of 209 at 4 nm above the bridge at the resonant wavelength 1612 nm. The magnetic and electric near-field distributions on the xz plane are depicted in Figure 6d,e. The maximum magnetic field enhancement of 5880 is obtained 2 nm below the metal bridge, where the electric field enhancement is 8100. Although the electromagnetic near field at this position is difficult to experimentally detect, it can be applied

for chemical and biosensing and nonlinear optics. The electric and magnetic field enhancement can be further improved by adding periodic grooves around the BBA antenna, which is described in the Supporting Information.

Compared to the existing nanostructures, which can produce an electromagnetic hot spot, the BBA antenna has apparent advantages. For the broken diabolo nanoantenna,[10] its field enhancement is much lower (1200 for the magnetic field and 1700 for the electric field). As to the broken-nanoring structure,[11] the field enhancement is also much smaller (180 for magnetic field and 280 for electric field), the excitation source is not common, and the structure composition is relatively complex. As for the capped nanoantenna,[9] its field enhancement is relatively lower (3000 for magnetic field and 1.6×10^4 for electric field) and its fabrication is quite complex and difficult.

■ CONCLUSION

In summary, we present the bridged bowtie aperture antenna, which can produce an electromagnetic hot spot. The optical nanocircuit theory is discussed to reveal its underlying mechanism. The BBA antenna samples with varied structural
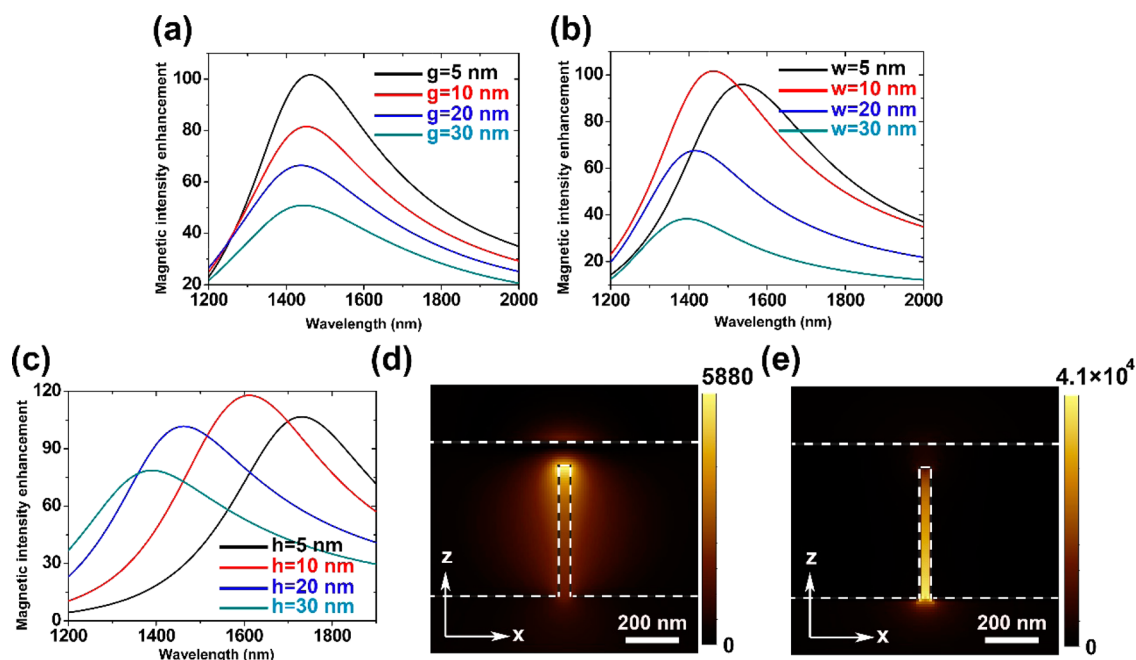
Figure 6. Magnetic field intensity enhancement dependence on (a) the bridge length g ($a = 210$ nm, $w = 10$ nm, $h = 20$ nm), (b) the bridge width w ($a = 210$ nm, $g = 5$ nm, $h = 20$ nm), and (c) the bridge thickness h ($a = 210$ nm, $g = 5$ nm, $w = 10$ nm). Normalized intensity distribution of (d) magnetic and (e) electric field in the xz plane at 1612 nm ($a = 210$ nm, $g = 5$ nm, $w = h = 10$ nm).

parameters are fabricated, and their electric near fields are visualized using s-SNOM. The magnetic near field of the BBA antenna is obtained based on Babinet's principle: its electromagnetic complement notched diabolo antenna is fabricated and the electric field of the NDA is measured using s-SNOM. This is the first work to experimentally verify the generation of such an electromagnetic hot spot. The BBA antenna shows apparent advantages over the existing nanostructures producing electromagnetic hot spots, which promise wide applications in nonlinear optics, biochemical sensing, and metamaterials.

■ METHODS

BBA Antenna Fabrication. The detailed fabrication process of the BBA antenna is shown in Supplementary Figure 3a. A layer of SiO_2 (thickness: 2 μm) and a layer of Si_3N_4 (thickness: 300 nm) are deposited respectively on the two sides of the Si wafer (thickness: 300 μm) using PECVD (Oxford System 100). Then a window (300 μm × 300 μm) is patterned by the photolithography system (SUSS MABA6), and the SiO_2 film in the window is removed by reactive ion etching (Oxford NGP80). After that, the bulk Si in the window is removed by inductively coupled plasma etching (Oxford ICP380) and KOH wet etching. Then a gold film (thickness: 60 nm) is deposited on the Si_3N_4 film by an e-beam evaporator (Lesker LAB18). After that, the BBA antenna is perforated on the Si_3N_4 film using a focused ion beam (FEI Helios Nanolab 650, 30KV, 1.1pA) with a fabrication resolution of 2 nm. Structural parameters of the antenna are controlled using ion scan path and ion dose as shown in Supplementary Figure 3b.

NDA Fabrication. The detailed fabrication process of the NDA is shown in Supplementary Figure 4a. A layer of electron resist poly(methyl methacrylate) (PMMA) is spin-coated on a SiO_2 substrate with a speed 4000 rpm to have a thickness of 400 nm and then baked at 180 °C for 5 min. Then a layer of 20 nm conducting resin is coated on the PMMA layer to solve the problem of charge accumulation during exposure. Then PMMA

is patterned using electron beam lithography (JEOL6300, 100 pA) and developed. A layer of gold (thickness: 60 nm) is then deposited using an e-beam evaporator. After that, the sample is immersed in acetone to lift off the unwanted area. Finally, the fabricated diabolo antenna sample is milled at its central area using focused ion beam (FIB) (FEI Helios Nanolab 650, 30 kV, 1.1 pA). Before FIB milling, a 5 nm layer of carbon is deposited on the sample to improve its conductivity. This layer is removed using reactive ion etching after the FIB milling. SEM images of the diabolo antenna and the NDA are shown in Supplementary Figure 4b−e.

Numerical Simulations. Numerical simulations in this work are conducted using commercial finite difference time domain software (Lumerical FDTD Solutions). Optical properties of gold are taken from Johnson and Christy.[48] A broadband plane wave with an electric component of 1 V/m and magnetic component of 0.00253 A/m is utilized. A 1 nm × 1 nm × 1 nm mesh size is used to maintain the simulation accuracy.

Transmission-Mode s-SNOM for Near-Field Mapping. As shown in Supplementary Figure 6, the transmission-mode s-SNOM (Neaspec s-SNOM) is based on an AFM working in tapping mode. An excitation laser at 1550 nm is incident upward on the sample with proper polarization. The near field scattered by the dielectric Si tip is collected and directed to a photodetector. The tip we use is a commercial Si probe (Arrow-NCR, Nanoworld) to avoid plasmonic coupling between the tip and the sample.[49] The radius of the tip apex is 10 nm to achieve high resolution, and the oscillation amplitude is 60 nm in our experiments. Higher harmonic demodulation and a pseudoheterodyne interferometer are used to extract the amplitude and phase signal from the background. By adjusting the half-wave plate in the interferometric path and the polarizer in front of the detector, we can obtain the near-field distribution of two orthogonal components E_p and E_s, which respectively are related to E_z and E_x in our experiments.

ASSOCIATED CONTENT

Ⓢ Supporting Information

The Supporting Information is available free of charge on the ACS Publications website at DOI: 10.1021/acsphotonics.6b00857.

Transmission dependence of the BBA antennas on its structural parameters; far-field radiation characteristics of the BBA antenna; schematic of the BBA antenna fabrication process; SEM images of fabricated BBA samples; schematic of the NDA fabrication process; SEM images of fabricated NDA samples; description of the BBA antenna with a bulls-eye structure; schematic of the transmission-mode s-SNOM system (PDF)

AUTHOR INFORMATION

Corresponding Authors

*E-mail (J.-R. Chu): jrchu@ustc.edu.cn.
*E-mail (X. Xu): xxu@ecn.purdue.edu.

ORCID Ⓘ

Jiaru Chu: 0000-0001-6472-8103

Notes

The authors declare no competing financial interest.

ACKNOWLEDGMENTS

REFERENCES

(1) Bharadwaj, P.; Deutsch, B.; Novotny, L. Optical antennas. *Adv. Opt. Photonics* **2009**, *1*, 438−483.

(2) Hecht, B.; Farahani, J.; Mühlschlegel, P.; Eisler, H. J.; Pohl, D. W.; Martin, O. J. F. Resonant optical antennas. *Science* **2005**, *308*, 1607−1609.

(3) Knight, M. W.; Sobhani, H.; Nordlander, P.; Halas, N. J. Photodetection with active optical antennas. *Science* **2011**, *332*, 702−704.

(4) Chen, Y.; Chu, J. R.; Xu, X. F. Plasmonic Multibowtie Aperture Antenna with Fano Resonance for Nanoscale Spectral Sorting. *ACS Photonics* **2016**, *3*, 1689−1697.

(5) Landau, L. D.; Bell, J.; Kearsley, M.; Pitaevskii, L.; Lifshitz, E.; Sykes, J. *Electrodynamics of Continuous Media*; Elsevier, 1984; Vol. 8.

(6) Grosjean, T.; Mivelle, M.; Baida, F.; Burr, G.; Fischer, U. Diabolo nanoantenna for enhancing and confining the magnetic optical field. *Nano Lett.* **2011**, *11*, 1009−1013.

(7) Zhou, N.; Kinzel, E. C.; Xu, X. Complementary bowtie aperture for localizing and enhancing optical magnetic field. *Opt. Lett.* **2011**, *36*, 2764−6.

(8) Liu, N.; Mukherjee, S.; Bao, K.; Li, Y.; Brown, L. V.; Nordlander, P.; Halas, N. J. Manipulating magnetic plasmon propagation in metallic nanocluster networks. *ACS Nano* **2012**, *6*, 5482−5488.

(9) Roxworthy, B. J.; Toussaint, K. C. Simultaneously tuning the electric and magnetic plasmonic response using capped bi-metallic nanoantennas. *Nanoscale* **2014**, *6*, 2270−2274.

(10) Yu, Z.; Gao, Z.; Wang, Z. Broken-diabolo nanoantenna for co-enhancing and-confining optical electric and magnetic field. *Opt. Commun.* **2015**, *346*, 34−37.

(11) Yu, P.; Chen, S.; Li, J.; Cheng, H.; Li, Z.; Tian, J. Co-enhancing and-confining the electric and magnetic fields of the broken-nanoring and the composite nanoring by azimuthally polarized excitation. *Opt. Express* **2013**, *21*, 20611−20619.

(12) Aouani, H.; Navarro-Cia, M.; Rahmani, M.; Sidiropoulos, T. P.; Hong, M.; Oulton, R. F.; Maier, S. A. Multiresonant broadband optical antennas as efficient tunable nanosources of second harmonic light. *Nano Lett.* **2012**, *12*, 4997−5002.

(13) Butet, J. r. m.; Thyagarajan, K.; Martin, O. J. Ultrasensitive optical shape characterization of gold nanoantennas using second harmonic generation. *Nano Lett.* **2013**, *13*, 1787−1792.

(14) Klein, M. W.; Enkrich, C.; Wegener, M.; Linden, S. Second-harmonic generation from magnetic metamaterials. *Science* **2006**, *313*, 502−504.

(15) Shalaev, V. M.; Cai, W.; Chettiar, U. K.; Yuan, H.-K.; Sarychev, A. K.; Drachev, V. P.; Kildishev, A. V. Negative index of refraction in optical metamaterials. *Opt. Lett.* **2005**, *30*, 3356−3358.

(16) Zhang, S.; Fan, W.; Panoiu, N.; Malloy, K.; Osgood, R.; Brueck, S. Experimental demonstration of near-infrared negative-index metamaterials. *Phys. Rev. Lett.* **2005**, *95*, 137404.

(17) Zhou, N.; Xu, X. Metamaterial-based perfect absorbers for efficiently enhancing near field radiative heat transfer. *J. Quant. Spectrosc. Radiat. Transfer* **2015**, *167*, 156−163.

(18) Xu, H.; Bjerneld, E. J.; Käll, M.; Börjesson, L. Spectroscopy of Single Hemoglobin Molecules by Surface Enhanced Raman Scattering. *Phys. Rev. Lett.* **1999**, *83*, 4357−4360.

(19) Ye, J.; Wen, F.; Sobhani, H.; Lassiter, J. B.; Dorpe, P. V.; Nordlander, P.; Halas, N. J. Plasmonic nanoclusters: near field properties of the Fano resonance interrogated with SERS. *Nano Lett.* **2012**, *12*, 1660−1667.

(20) Thyagarajan, K.; Butet, J. r. m.; Martin, O. J. Augmenting second harmonic generation using Fano resonances in plasmonic systems. *Nano Lett.* **2013**, *13*, 1847−1851.

(21) Zhang, Y.; Wen, F.; Zhen, Y.-R.; Nordlander, P.; Halas, N. J. Coherent Fano resonances in a plasmonic nanocluster enhance optical four-wave mixing. *Proc. Natl. Acad. Sci. U. S. A.* **2013**, *110*, 9215−9219.

(22) Meinzer, N.; Barnes, W. L.; Hooper, I. R. Plasmonic meta-atoms and metasurfaces. *Nat. Photonics* **2014**, *8*, 889−898.

(23) Yu, N.; Capasso, F. Flat optics with designer metasurfaces. *Nat. Mater.* **2014**, *13*, 139−50.

(24) Anker, J. N.; W Paige, H.; Olga, L.; Shah, N. C.; Jing, Z.; Van Duyne, R. P. Biosensing with plasmonic nanosensors. *Nat. Mater.* **2008**, *7*, 442−53.

(25) Chihhui, W.; Khanikaev, A. B.; Ronen, A.; Nihal, A.; Ahmet Ali, Y.; Hatice, A.; Gennady, S. Fano-resonant asymmetric metamaterials for ultrasensitive spectroscopy and identification of molecular monolayers. *Nat. Mater.* **2011**, *11*, 69−75.

(26) Chen, Y.; Chen, J.; Xu, X.; Chu, J. Fabrication of bowtie aperture antennas for producing sub-20 nm optical spots. *Opt. Express* **2015**, *23*, 9093−9099.

(27) Alù, A.; Engheta, N. Input Impedance, Nanocircuit Loading, and Radiation Tuning of Optical Nanoantennas. *Phys. Rev. Lett.* **2008**, *101*.

(28) Alù, A.; Engheta, N. Tuning the scattering response of optical nanoantennas with nanocircuit loads. *Nat. Photonics* **2008**, *2*, 307−310.

(29) Schuck, P.; Fromm, D.; Sundaramurthy, A.; Kino, G.; Moerner, W. Improving the mismatch between light and nanoscale objects with gold bowtie nanoantennas. *Phys. Rev. Lett.* **2005**, *94*, 017402.

(30) Lorente-Crespo, M.; Wang, L.; Ortuño, R. n.; García-Meca, C.; Ekinci, Y.; Martínez, A. Magnetic hot spots in closely spaced thick gold nanorings. *Nano Lett.* **2013**, *13*, 2654−2661.

(31) Huang, Z.; Xue, J.; Hou, Y.; Chu, J.; Zhang, D. Optical magnetic response from parallel plate metamaterials. *Phys. Rev. B: Condens. Matter Mater. Phys.* **2006**, *74*, 193105.

(32) Sarychev, A. K.; Shvets, G.; Shalaev, V. M. Magnetic plasmon resonance. *Phys. Rev. E* **2006**, *73*, 036609.

(33) Hillenbrand, R.; Keilmann, F. Complex optical constants on a subwavelength scale. *Phys. Rev. Lett.* **2000**, *85*, 3029−32.

(34) Ocelic, N.; Huber, A.; Hillenbrand, R. Pseudoheterodyne detection for background-free near-field spectroscopy. *Appl. Phys. Lett.* **2006**, *89*, 101124.

(35) Olmon, R. L.; Rang, M.; Krenz, P. M.; Lail, B. A.; Saraf, L. V.; Boreman, G. D.; Raschke, M. B. Determination of electric-field, magnetic-field, and electric-current distributions of infrared optical antennas: a near-field optical vector network analyzer. *Phys. Rev. Lett.* **2010**, *105*, 167403.

(36) Grosjean, T.; Ibrahim, I. A.; Suarez, M. A.; Burr, G. W.; Mivelle, M.; Charraut, D. Full vectorial imaging of electromagnetic light at subwavelength scale. *Opt. Express* **2010**, *18*, 5809−24.

(37) Schnell, M.; Garcia-Etxarri, A.; Alkorta, J.; Aizpurua, J.; Hillenbrand, R. Phase-resolved mapping of the near-field vector and polarization state in nanoscale antenna gaps. *Nano Lett.* **2010**, *10*, 3524−8.

(38) Burresi, M.; Oosten, D. V.; Kampfrath, T.; Schoenmaker, H.; Heideman, R.; Leinse, A.; Kuipers, L. Probing the magnetic field of light at optical frequencies. *Science* **2009**, *326*, 550−3.

(39) Kihm, H. W.; Kim, J.; Koo, S.; Ahn, J.; Ahn, K.; Lee, K.; Park, N.; Kim, D. S. Optical magnetic field mapping using a subwavelength aperture. *Opt. Express* **2013**, *21*, 5625−33.

(40) Denkova, D.; Verellen, N.; Silhanek, A. V.; Valev, V. K.; Van, D. P.; Moshchalkov, V. V. Mapping magnetic near-field distributions of plasmonic nanoantennas. *ACS Nano* **2013**, *7*, 3168−76.

(41) Feber, B. L.; Rotenberg, N.; Beggs, D. M.; Kuipers, L. Corrigendum: Simultaneous measurement of nanoscale electric and magnetic optical fields. *Nat. Photonics* **2013**, *8*, 43−46.

(42) B, Ö.; Vogelgesang, R.; Sigle, W.; Talebi, N.; Koch, C. T.; van Aken, P. A. Hybridized metal slit eigenmodes as an illustration of Babinet's principle. *ACS Nano* **2011**, *5*, 6701−6.

(43) Hentschel, M.; Weiss, T.; Bagheri, S.; Giessen, H. Babinet to the half: coupling of solid and inverse plasmonic structures. *Nano Lett.* **2013**, *13*, 4428−4433.

(44) Zentgraf, T.; Meyrath, T. P.; Seidel, A.; Kaiser, S.; Giessen, H. Babinet's principle for optical frequency metamaterials and nano-antennas. *Phys. Rev. B* **2007**, *76*, 3407.

(45) Yang, H. U.; Olmon, R. L.; Deryckx, K. S.; Xu, X. G.; Bechtel, H. A.; Xu, Y.; Lail, B. A.; Raschke, M. B. Accessing the Optical Magnetic Near-Field through Babinet's Principle. *ACS Photonics* **2014**, *1*, 894−899.

(46) Hongcang, G.; Meyrath, T. P.; Thomas, Z.; Na, L.; Liwei, F.; Heinz, S.; Harald, G. Optical resonances of bowtie slot antennas and their geometry and material dependence. *Opt. Express* **2008**, *16*, 7756−7766.

(47) Raether, H. *Surface Plasmons on Smooth Surfaces*; Springer, 1988.

(48) Johnson, P. B.; Christy, R.-W. Optical constants of the noble metals. *Phys. Rev. B* **1972**, *6*, 4370.

(49) Esteban, R.; Vogelgesang, R.; Kern, K. Tip-substrate interaction in optical near-field microscopy. *Phys. Rev. B: Condens. Matter Mater. Phys.* **2007**, *75*, 195410.